HOVER PERFORMANCE AND BOUNDARY LAYER MEASUREMENTS OF LOW REYNOLDS NUMBER ROTORS

Christopher G. Cameron, U.S. Army DEVCOM AvMC, Moffett Field, USA
Joon W. Lim, Army DEVCOM AvMC, Moffett Field, USA
Shai Alexandroni, Israeli Aerospace Industries, Lod, Israel
Yonatan Klein, Israeli Aerospace Industries, Lod, Israel
Danny Abramov, Israeli Aerospace Industries, Lod, Israel
Jeremy Shipman, Combustion Research and Flow Technology Inc., Pipersville, USA
Timothy Weathers, Combustion Research and Flow Technology Inc., Pipersville, USA

Abstract

Two teams optimized low Reynolds number rotors with the goal of improving hover and loiter performance of a small commercial off the shelf quadrotor unmanned aerial system. The resulting rotors were constructed and tested against the baseline system hover. The optimized rotors achieved 6% and 3% increases in figure of merit at the design 1.5 lbf thrust in hover, while carefully chosen boundary layer trips improved low RPM performance of one optimized rotor. IR thermography identified the qualitative location and extent of laminar separation bubbles and turbulent transition on the upper rotor surface. The IR images reveal large differences in the boundary layer structure between the baseline and two optimized rotors, with separation and reattachment occurring further forward and over a smaller chordwise extent in the optimized rotors. After optimization, a mid-fidelity lifting line coupled vortex particle code and high-fidelity Helios CFD code were used to simulate the baseline and one optimized rotor system.

1. NOTATION[1]

Symbols

A	Rotor disk area, πR^2
c	Local airfoil chord [in]
cd	Airfoil drag coefficient
cl	Airfoil lift coefficient
cm	Airfoil moment coefficient
C_T	Rotor thrust coefficient $\frac{T}{\rho A\Omega^2 R^2}$
C_Q	Rotor torque coefficient $\frac{Q}{\rho A\Omega^2 R^3}$
$I^{(r,x)}$	IR raw intensity at rotor location (r,x)
I_N	Infrared intensity with global normalization
I_r	Infrared intensity with local radius normalization
L	Rotor wind-axis lift
r	Radial station [in]
R	Rotor radius [in]
Re	Reynolds Number
T	Thrust [lbf]
Q	Torque [lbf-in]
x	Chordwise station [in]
ρ	Air density [slug/ft^3]
σ	solidity
σ_T	Thrust-weighted solidity
Ω	Rotor angular velocity rad/s

Acronyms:

FM	Figure of Merit
IR	Infrared
LE	Leading edge
LD_e	Effective lift to drag ratio
LSB	Laminar Separation Bubble
NURBS	Non-Uniform Rational B-Spline
RPM	Revolutions per minute
TE	Trailing edge
UAS	Unmanned aerial system

2. INTRODUCTION

Group 1 (Ref. 1) rotary wing unmanned aerial systems, weighing less than 21 lb, often employ fixed pitch variable RPM rotors which operate at chord-based Reynolds numbers (Re) on the order of 100,000. Here boundary layer dynamics change rapidly, transitioning from low Re where thin airfoils with sharp leading edges provide best performance, to a regime where more traditional airfoil designs with smooth surfaces are effective (Ref. 2, 3). Modeling and design of these rotors is especially challenging, as small discrepancies in predicted transition and separation cause large performance swings. The present paper explores the design and hover testing of two rotors optimized for hover and forward flight performance at Reynolds numbers between 75,000 and 100,000.

Design studies for low Reynolds number rotors have tended to cover Reynolds number regimes an order of magnitude or more less than the 100,000 baseline in the present study. Example target applications include micro-aerial vehicles weighing less than 100 g (Ref. 4, 5) and designs for Martian exploration where the extreme low-density atmosphere keep Reynolds less than 10,000 (Ref. 6). The challenges in these regimes are distinct from those at higher, intermediate Reynolds number, with designs incorporating extremely thin airfoils and sharp leading edges to induce unsteady leading edge flow separation. In the Reynolds number range relevant to the current study, a significant body of work exists focusing on design optimization of airfoils for fixed wing applications ranging from hobbyist gliders, to UAS and human powered applications (Ref. 7). The design of airfoils in these regimes focuses on control of the laminar separation bubble (LSB), either through external trips or passive design features, known as transition ramps(Ref. 8–10).

Given the importance of the LSB to airfoil performance in this regime measurements of the boundary layer state help provide insight into the rotor performance. For small UAS boundary layer measurements have historically been difficult given the small scale of the rotors and sensitivity to flow disturbances. Infrared thermography has recently become a staple measurement technique for steady and unsteady rotor boundary layer measurements with the advent of high-speed, low-noise IR cameras. Thermography is a non-intrusive optical technique which has been used to measure boundary layer state and transition in non-rotating applications since the first availability of spatially resolved temperature measurements. It leverages the Reynolds analogy between heat and momentum transport in the boundary layer to relate blade surface temperature to coefficient of friction. A comprehensive overview of recent developments in IR transition measurements with a focus on rotary wing applications is given by Wolf et al (Ref. 11).

Several different approaches to IR measurement have emerged. At higher Reynolds number studies have used forced heating, both internal (Ref. 12), and external (Ref. 13), or have used novel optical setups to extend integration time and make measurements using only aerodynamic heating in the boundary layer itself (Ref. 14). Recent studies of rotors operating near Reynolds Numbers of 100 thousand have seen success using both transient and steady heating from external lamps or laser diodes (Ref. 15, 16). Additional studies incorporating multiple measurement techniques have validated the connection between IR thermography and boundary layer state including work on rotors a high Reynolds number (Ref. 17). At lower Reynolds number Wynnychuk and Yarusevych used particle image velocimetry imaging to validate separation, transition and reattachment points measured from IR surface temperature distributions and their chordwise derivatives on a 2D airfoil section(Ref. 18).

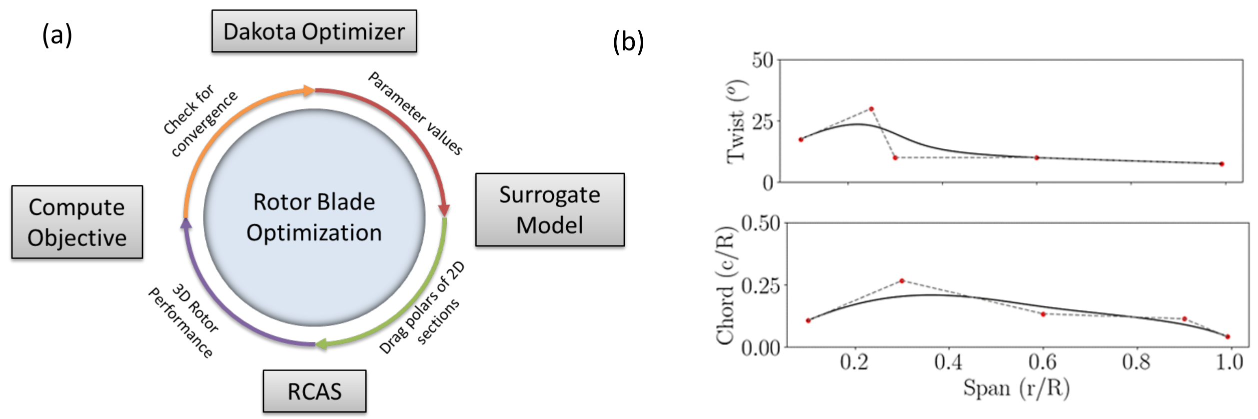

Figure 1. (a) CRAFT Tech rotor optimization framework flowchart (b) Example parameterization of twist and chord degrees of freedom with NURBS control points

This paper uses a purpose-built hover test stand and IR thermography techniques to compare the performance and boundary layer structure of three rotors, one baseline and two optimized each using a different tool chain developed as part of the United States – Israel Rotorcraft Project Agreement. The optimized designs rely on airfoils which control the laminar separation bubble. IR thermography allows interrogation of the state of the boundary layer providing a deeper understanding of the measured performance differences between baseline and optimized rotors. Finally, the performance results are compared to a mid-fidelity lifting line/vortex particle model as well as high fidelity CFD simulations to assess accuracy in this Reynolds number regime.

3. ROTOR DESIGN OPTIMIZATION

The Gen 2 T-Motor 15x5 carbon fiber rotor, from the SUI Endurance quadcopter, was chosen as the baseline optimization target given the volume of historical experimental and computational studies on the vehicle (Ref. 19–22). The rotor optimization conditions were based on nominal hover and forward flight conditions as summarized in Table 1. Forward flight trim conditions were taken from prior full-vehicle wind tunnel tests conducted by Russell et al. (Ref. 19).

The objective functions chosen for maximization were figure or merit in hover, and effective lift to drag ratio in forward flight defined in equations 1 and 2 below. Additional blade root geometry and minimum thickness constraints are included based on feedback from the blade manufacturer. Both optimization processes employ low Reynolds number airfoil profiles optimized and tested in a previous phase of the joint project and impose a local margin to maximum airfoil cl based on the baseline T-Motor blade to ensure equivalent stall margin to the baseline system (Ref. 23). At 75% radius this translates to a cl stall margin of 0.55.

Table 1. SUI Endurance vehicle parameters and optimization constraints

Parameter	
Weight	6.0 lbf
Number of Rotors	4
Rotor Diameter	15 in
Number of Blades	2
Cruise Speed	5 m/s

$$FM = \frac{C_T^{(3/2)}}{\sqrt{2}C_Q} \quad (1)$$

$$\mathrm{LD_e} = \frac{LV_{inf}}{\Omega Q} \quad (2)$$

3.1. CRAFT Tech Rotor

The 3D rotor optimization process for the Combustion Research and Flow Technologies Inc. (CRAFT Tech) rotor is outlined in Figure 1a. It uses a design philosophy based on a search-based design optimization framework using evolutionary algorithms. A multi objective genetic algorithm approach was implemented using Sandia National Laboratories' Dakota code(Ref. 24). Objectives for each design were

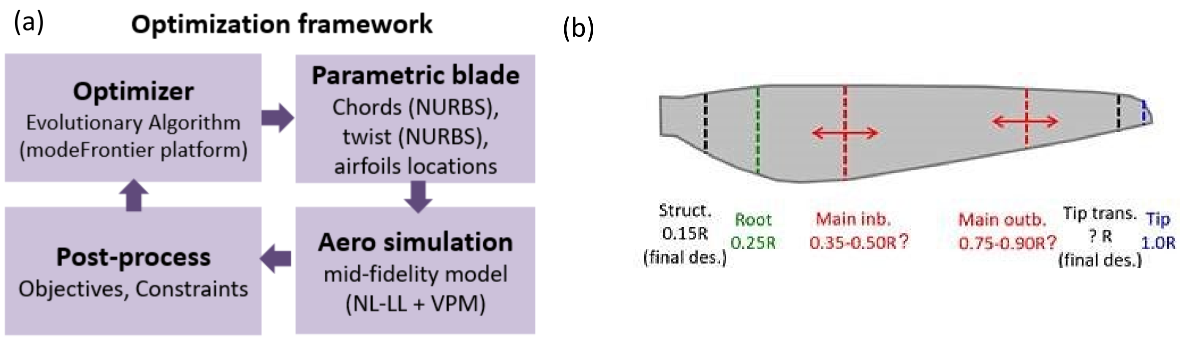

Figure 2. (a) IAI optimization flowchart (b) Airfoi section distributions showing the two transition locations used as optimization intputs: Main-Inboard and Main-Outboard

computed for a hover condition and cruise condition. The initial population size was 150 designs created randomly from the design space while enforcing uniqueness. The optimization parameterization used 19 degrees of freedom. Rotor chord and twist are parameterized as B-splines with 6 degrees of freedom each. An airfoil family was created using parametrically similar airfoils. Each airfoil is uniquely characterized by the max airfoil thickness. The airfoil geometry at 7 span locations defines the last 7 degrees of freedom in the optimization framework.

The airfoil lift and drag polars are generated on-demand from a deep-learning based surrogate model trained on over 3000 CFD calculations and tested on a set of 300 independent cases. CFD simulations for the training and validation cases were run using OVERFLOW with the Coder Amplification Transport turbulence transition model (Ref. 25). The machine learning model to predict performance of the airfoils was written in PyTorch (Ref. 26) and trained on a GPU. A linear regressor with three hidden layers was used for the PyTorch model. The input layer has three inputs: the Reynolds number, angle of attack, and thickness. The output layer has three outputs: cl, cd, and cm. The hidden layers have 300, 200, and 300 neurons, respectively with rectified linear unit (ReLU) activation functions applied to them.

Rotor performance is calculated using the blade element modeling software RCAS (Ref. 27) with a prescribed inflow model. The optimization framework was run on 192 processors over 3 days. A total of 24,000 designs were analyzed over 94 generations

3.2. IAI Rotor

The Israeli Aerospace Industries (IAI) rotor optimization is structured in a similar manner as shown in Figure 2a. The core optimization routine uses the NSGA-II multi-objective evolutionary algorithm implemented in the commercial software modeFrontier (Ref. 28). Rotor geometry was parametrized by NURBS with 8 degrees of freedom each for chord and twist. In contrast to the CRAFT Tech methodology, the IAI rotor incorporates three airfoils – root, main and outboard – which were derived from the previously optimized section. The transitions between the root, mid-span and tip airfoils were an additional two degrees of freedom in the optimizer as shown in Figure 2b.

An in-house, mid-fidelity simulation code based on the open-source DUST (Ref. 29) vortex particle wake model was used to calculate rotor performance. Simulations used 40 time steps per revolution with a total run-time of 12 revolutions for convergence in hover. The lifting line model was discretized into 31 radial segments with a single VPM particle emitted from each aerodynamic section per timestep (up to a maximum of 10 million particles). The lift and drag polars for the airfoil sections were calculated using MSES (Ref. 30) with free transition and Ncrit=7.4.

3.3 Final Designs

Final optimized designs are shown in Figure 3 along with the baseline rotor. A difference in the implementation of the root geometry constraint allowed the CRAFT Tech optimization to drive toward a large inboard chord, likely in an effort to increase Reynolds number. Beyond 70% span all three rotors collapse onto similar, near linear taper rates out to the blade tip. The CRAFT Tech rotor exhibits an approximately bi-linear twist distribution decreasing from root to tip with the exception of a small constant section between 60 and 80% span. The IAI design features increasing in twist to a maximum of 18.8 degrees at 40% radius before decreasing from 50% span to the tip.

Table 2 shows the final solidity and thrust weighted solidity of the baseline and optimized rotor designs. The IAI design increases thrust weighted solidity by 8% while the CRAFT Tech rotor increases by 15%. This solidity increase and aggressive twist distributions of both rotors, in concert with the highly cambered airfoil sections, suggest that the optimizers in both cases have driven toward rotors designed to operate at higher thrust coefficients and therefor lower RPM and Reynolds number than the baseline rotor.

Table 2. Baseline and optimized rotor solidities

	Baseline	**IAI**	**CRAFT**
σ	0.069	0.080	0.090
σ_T	0.072	0.078	0.083

4. EXPERIMENTAL AND COMPUTATIONAL SETUP

Experiments were conducted in the U.S. Army Hover Chamber located at NASA Ames. The test stand is at the center of the 27- by 24-foot room. The 15-inch diameter rotor is located is 8 feet above the floor and approximately 15 feet below the ceiling. All results are presented with the rotor configured to thrust down, sending the wake towards the ceiling. This configuration was found to minimize recirculation and ground effect, with the rotor separated approximately 10 diameters from the effective ground plane. The data for each rotor was compiled from multiple runs spread over multiple days and months to account for statistical uncertainty over multiple time scales. Sweeps were performed starting from 1000 RPM with 500 RPM steps. A total of 10 data points were collected at each RPM during the sweep, 5 during the sweep up and 5 during the sweep down. Repeat points at nominal 1.5 lbf thrust were taken for each design in separate runs of 15 points each.

4.1. Instrumentation

The rotor test stand is shown in Figure 4. Instrumentation was selected based on the expected baseline rotor operating point of 1.5 lbf thrust and 1.1 lbf-in Torque, with a target propagated figure of merit uncertainty of less than 1% at the nominal 1.5 lbf thrust condition. Loads are measured using individual thrust (Interface SML-10) and torque (Futek TFF325) load cells mounted in series. The motor is mounted on a phenolic spacer for thermal isolation and incorporates a 1024/rev incremental encoder for measuring speed and triggering optical

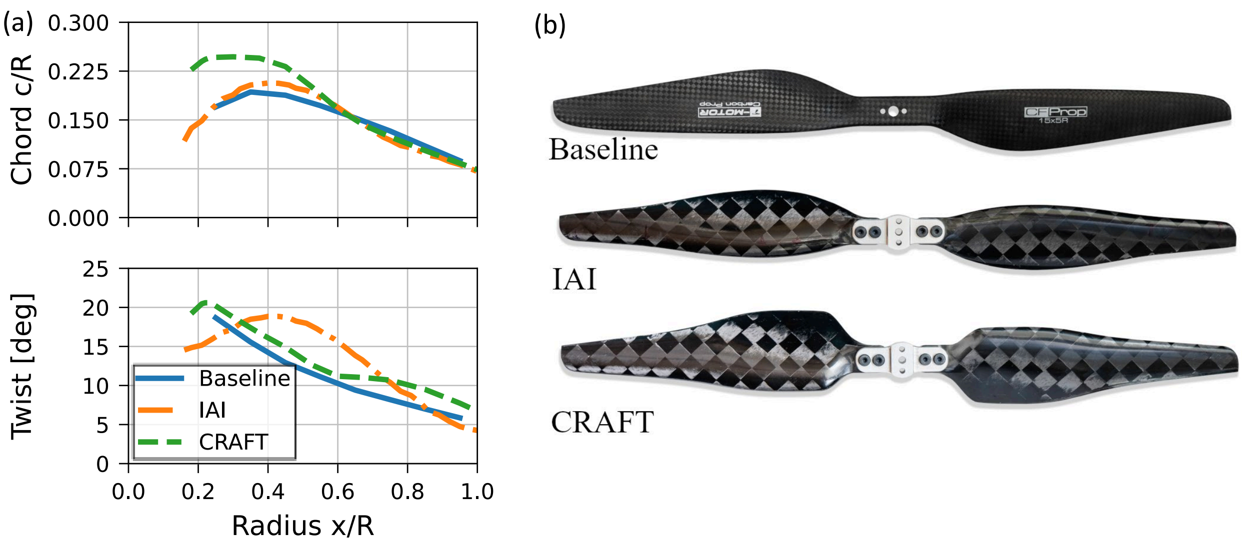

Figure 3. (a) Spanwise chord and twist distributions of the baseline and optimized rotors (b) Baseline rotor and optimized rotors, note aluminum hub for root pitch adjustments

measurements. In-situ check loads and external shunt calibrations were performed after installation. Additional shunt calibrations internal to the data acquisition system were performed prior to each data run to correct for any sensitivity changes over time. Data was collected using NI PXIe 4339 24-bit bridge modules simultaneously sampled at 10 kHz.

4.2. Infrared Measurements

A FLIR X8501SC-SLS camera was used to capture temperature distributions of the rotor upper surfaces at 1000, 2000 and 3000 RPM. The Strained Layer Superlattice (SLS) sensor response extends into the long wave infrared range providing excellent performance near room temperature. Using a 50 mm f2.3 lens the rotor blade was imaged on a 576x256 pixel window. With this lens the image per-pixel resolution was 0.18% of the blade radius and between 1.2% and 1.3% of the rotor chord at 75% span. The test stand incremental encoder was used to trigger image acquisition once-per-revolution, effectively freezing the rotor blade in-place. Integration time was fixed at 58 microseconds and the resulting motion blur at the blade-tip varied from approximately 0.045” at 1000 RPM to 0.13” at 3000 RPM, between approximately 5 and 15 percent of tip chord respectively.

Initial efforts to image the bare carbon-fiber blades were unsuccessful, with distinctive checkerboard patterns left by the varying fiber angles of the woven fabric. A matte black enamel-based paint was applied to the blades eliminating the issues with fabric directivity. Data presented in this paper follows a combination of acquisition techniques described in the literature. Like Thiessen and Schulein (Ref. 15) unheated reference images were first taken for each rotor at the target operating RPMs. These reference images help correct for radially varying aerodynamic heating near the blade-tips due the rotor angular velocity.

Next, externally heated images were captured using a 500 Watt xenon spot lamp. A single rotor blade was aligned with the spotlight and 60 seconds of pre-heating was applied before spinning the rotor to the target velocity, similar to Jaroslwaski et al.(Ref. 16). Images were acquired for 500 revolutions

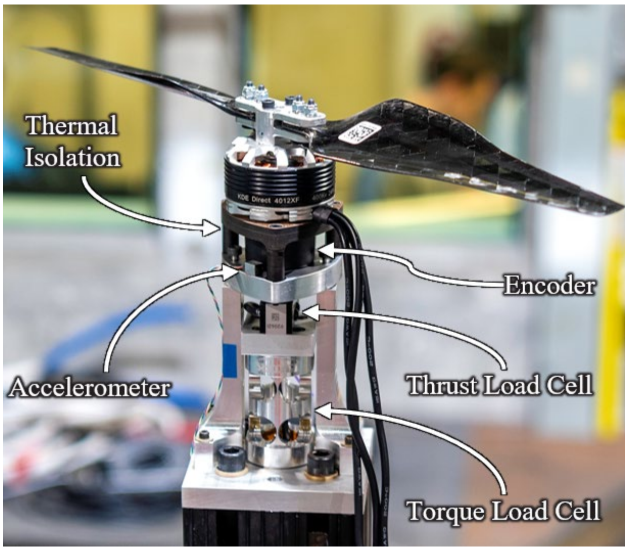

Figure 4. Test stand and instrumentation, rotor to send wake upwards and orient lower blade surface toward IR camera

capturing the transient temperature decay as the rotor was convectively cooled. Blade surface temperatures ranged between 10 C and 2 C above the ambient temperature which varied between 15 and 20 C. This provided sufficient contrast while avoiding adverse effects on flow transition.

Processing began with background subtraction to generate a masked blade image. The sets of 500 heated and unheated images were then averaged and subtracted from one another, generating maps of temperature rise from external heating. A two-dimensional moving average filter with spanwise and chordwise widths of 8 and 2 pixels (approximately 1.4% radius and 2.5% chord) was then applied to further reduce noise through local spatial averaging. Finally, the temperature rise values were normalized onto the interval [0,1] for relative comparison between runs. The boundary layer structure is revealed by these relative intensity differences without the need for a time-consuming absolute temperature calibration of each test article.

4.3. Computational Models

Results are presented for a mid-fidelity computational model used during the IAI optimization process. It combines a non-linear lifting line model with MSES generated airfoil lookup tables with the DUST lifting line VPM model. Details are described in

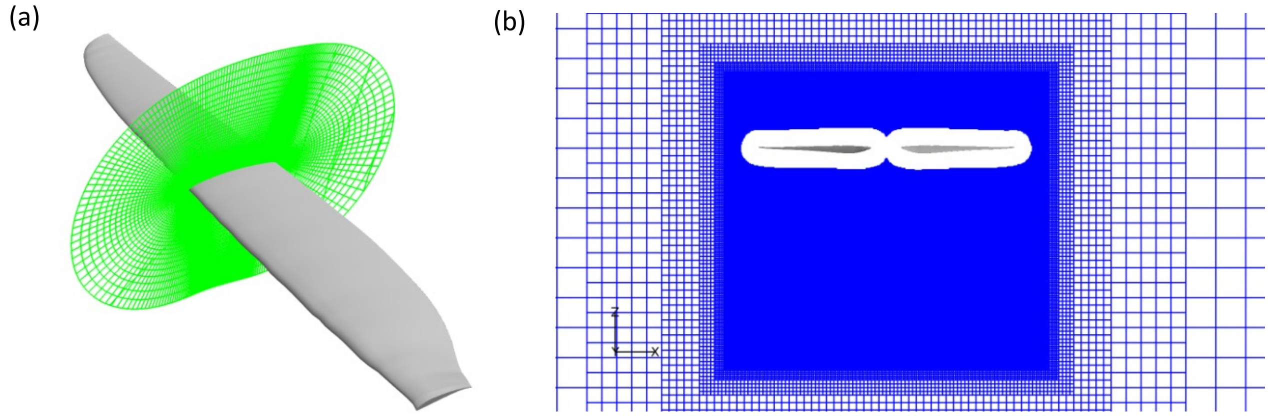

Figure 5. (a) Near-body mStrand mesh (b) Off-body CFD meshes showing refinement levels close to the rotor

section 3.2. In addition, a high fidelity CFD model was run for both the baseline and IAI rotors described below.

4.3.1. Computational Fluid Dynamics

The Helios CFD solver used in this study consists of two parts: a near-body solver that models and resolves the flow field near the solid bodies and an off-body solver that resolves the wake structures. The Unsteady Reynolds Averaged formulation of the Navier-Stokes equations (URANS) and their detached eddy simulation (DES) variants are usually employed to create an approach that balances efficiency and accuracy towards achieving practical simulations of rotorcraft systems. Helios supports a suite of near-body solvers (structured grid, unstructured grid or strand-based grid) that can operate in tandem within the same framework. The off-body solver in Helios uses a low dissipation high-order finite difference method that can transport and preserve wake structures and hence provide improved accuracy for aerodynamic interaction calculations. The detailed descriptions of various modules in Helios can be found in (Ref. 31).

Helios mStrand (Ref. 32) is used for near-body solver in the present study. mStrand is a specialized strand grid solver that uses a vertex-centered finite-volume spatial discretization. The Reynolds-averaged Navier-Stokes (RANS) equations in a general moving coordinate system are solved. mStrand accommodates both quadrilateral and triangular surface elements and handles general prismatic meshes in the normal (strand) direction. The solver incorporates a second-order implementation of full Navier-Stokes for the viscous terms (no thin-layer approximation) and the option of using the Spalart-Allmaras (SA) or the Menter's k-ω SST turbulence models implemented with a first order discretization. In the present study, a fully-turbulent SA-DES (Detached Eddy Simulation) was employed.

Figure 5a shows a cut through of the rotor blade volume mesh at r/R=0.7. Rotor has two blades, and each blade has a grid of 249 points around the airfoil and 189 points along blade span with extending 1c in the strand direction using 101 points where c is the mean chord (= 0.0272m or 1.07in). The resulting rotor grid points are 12.5 million points including fringe points.

The off-body grids have 10 levels in grid refinement, extending 147R in each direction to avoid the effect of freestream boundaries. The fixed refinement box with a mesh size of 0.0486c is defined in [-1.2R, 1.2R; -1.2R, 1.2R; -1.67R, 0.53R]. The finest mesh size of the off-body grids near the rotor about 0.0486c (see Figure 5b) The off-body grid contains 86.7 million grid points including fringe points. In the present analysis, a 0.25-degree time step was used with a SA-DES turbulence model.

Hover runs were run over 15 full rotor revolutions with a total of 21,600 time steps. Each run took about 129 hours using DoD High Performance Computing (HPC) Carpenter 576 cores (3 nodes x 192 cores).

5. RESULTS

Tests were run in two blocks three months apart. The first set of tests focused on performance measurement for all rotor configurations and trip configurations as well as studies on test procedure and installation effects. The second set of tests focused on IR measurements of the rotors including repeat performance measurements to examine long-term measurement uncertainty.

5.1. Measured Performance

The data presented below is compiled from all measurement runs including both early performance measurements, as well as later IR measurements. Error bars in the subsequent plots are ± 95% of the mean including both point-to-point statistical variation as well as fixed calibration uncertainties propagated through the equations for derived quantities such as figure of merit or thrust coefficient.

5.1.1. Clean Rotors

The primary goal of the experiments was confirming rotor performance at the hover optimization target of 1.5 lbf thrust. These results are summarized in Table 3. Both designs show figure of merit improvements over baseline, with 3% for the CRAFT Tech rotor and 6% for the IAI rotor. The increased solidity and airfoil design lift coefficient are reflected in the much larger thrust and torque coefficients of the IAI and CRAFT Tech rotors, along with an approximately 20% reduction in RPM. The resulting nominal Reynolds numbers at 75% span are 25-30% lower than the baseline rotor, indicating the high efficiency of the airfoil designs incorporated into the optimized rotors. Both the IAI and designs are operating at significantly higher blade loadings than the baseline rotor, 33% and 25% respectively. This despite the increased solidity of the optimized rotors.

Table 3. Measured baseline and optimized rotor performance at the design nominal thrust of 1.5 lbf

	Baseline	IAI	CRAFT
FM	0.671±0.008	0.710±0.008	0.692±0.008
RPM	3712 ± 12	3033 ± 16	3068 ± 7
$Re_{75}x10^3$	97.4 ± 0.4	71.9 ± 0.4	74.4 ± 0.2
$CTx10^3$	8.7 ± 0.1	13.0 ± 0.2	12.5 ± 0.2
$CQx10^3$	0.86 ± 0.01	1.48 ±0.02	1.43 ±0.02
CT/σ_T	0.121±0.001	0.167±0.003	0.151±0.002

Figure 6 shows figure of merit plotted vs nominal thrust level. The optimized rotors outperform the baseline rotor across all thrust levels, with the largest margins occurring between 0.5 and 1.0 lbf thrust. While the optimized rotor figure of merit levels out past the design point of 1.5 lbf thrust, the baseline rotor continues to improve as RPM and Reynolds number increase.

The trends in figure of merit seen in Figure 6 arise solely due to the change in Reynolds number as RPM increases, so it makes sense to examine rotor performance vs Reynolds number directly. These trends of figure of merit as well as thrust and torque coefficient are plotted in Figure 7a-c. The increase in optimized rotor performance at a given Reynolds number is larger than the gap at a given thrust. Similar trends in thrust coefficient are seen for all three rotors, despite the large gap in absolute value between the baseline and optimized designs. Thrust

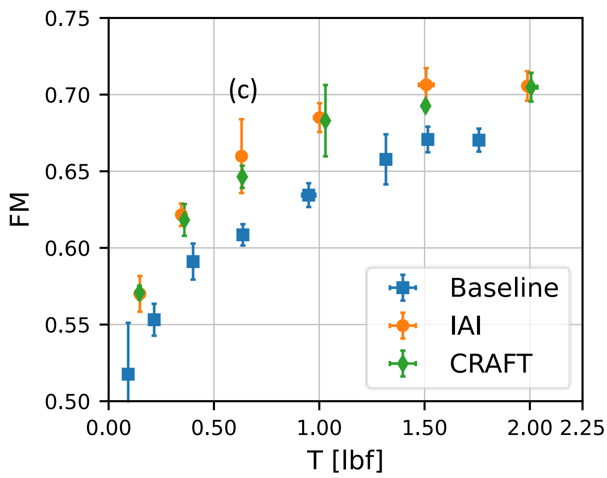

Figure 6. Measured figure of merit vs thrust for the baseline and optimized rotors

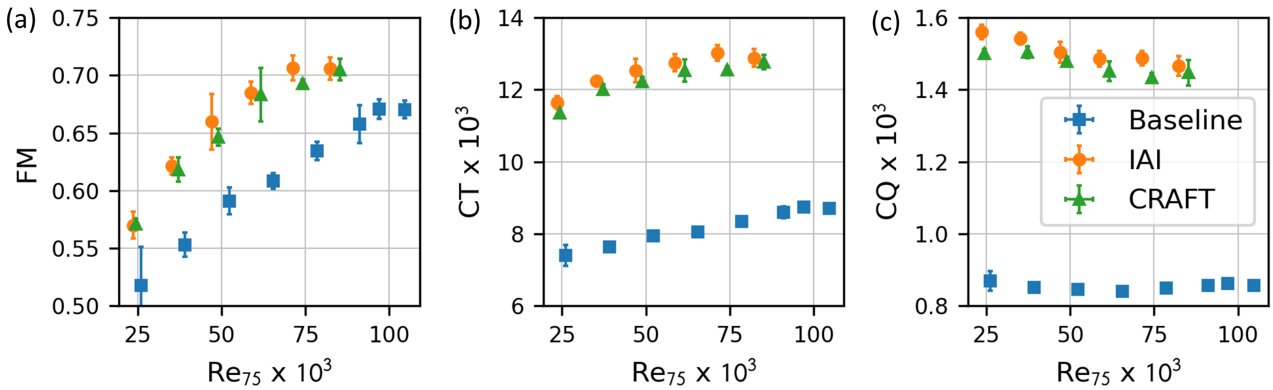

Figure 7. Comparison of baseline and clean optimized rotors (a) Figure of merit vs. Reynolds Number (b) Thrust coefficient vs Reynolds number (c) Torque coefficient vs. Reynolds number

coefficient rises with Reynolds number, before leveling out near Reynolds numbers of 75,000 for the optimized rotors and 100,000 for the baseline rotor.

Torque coefficient stays relatively constant with Reynolds number for the baseline rotor but falls for the optimized designs. Like thrust coefficient, the torque coefficients of the optimized rotors levels out near Reynolds number of 75,000, while there is a slight rise for the baseline rotor near 100,000.

5.1.2. Boundary Layer Trips

A series of boundary layer trips were applied to the IAI rotor. These trip configurations were selected based on pre-test calculations of the boundary layer structure taken from MSES. The trips were constructed from thin adhesive tapes cut into 0.059” chordwise strips, forming two-dimensional trips. The trips were applied in three radial segments: an inboard segment running from the root to 25% span, a mid-span segment from 40% to 75% span, and an outboard segment from 75% span to the blade tip. The three segments allow the thickness of the trip to be varied based on the local boundary layer thickness. The inner and mid-span trips were applied 20% aft of the leading edge, while the outboard trip varied between 20% chord at 75% span and 10% chord at the blade tip. Figure 8 shows a blade with trips applied to all three segments.

A total of 11 trip configurations were investigated with thicknesses ranging between 0.005” and 0.00075”. Data is presented here for two configurations described in Table 4. The first configuration, trip #1, consisted of the thickest, most aggressive trips tested. The second configuration, trip #5 left the blade tip region un-tripped and resulted in the best compromise of performance across the Reynolds number range.

Table 4. IAI rotor trip thicknesses in inches

	Inner	Mid-Span	Outer
Trip 1	0.005	0.002	0.0015
Trip 5	0.003	0.0015	None

The variation of figure of merit, thrust coefficient and torque coefficient for the tripped configurations are compared to the un-tripped IAI configuration in Figure 9. Trip #1 shows a large increase in performance at low Reynolds numbers before falling below the clean rotor performance above Reynolds numbers of 60,000. Trip #5 shows a smaller improvement at low Reynolds number but matches the clean rotor performance all the way to the maximum rotor speed.

Examining the trends in thrust and torque coefficient we see that the performance benefit at low Reynolds numbers is primarily due to an increase in CT, outweighing a corresponding increase in torque coefficient. Similarly, the penalty for trip #1 at higher Reynolds numbers is largely due to a drop in CT relative to the clean configuration.

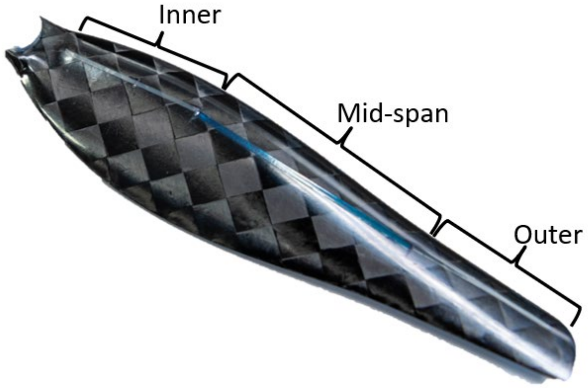

Figure 8. Two-dimensional boundary layer trips applied to the IAI blade using adhesive tape. Thickness varies across three spanwise segments

5.2. IR Measurements

IR measurements were performed at 1000, 2000 and 3000 RPM for all three rotors covering a Reynolds number range of approximately 25,000 to 75,000 at 75% span. Data is presented using two different normalizations of the temperature rise between heated and unheated images. The first is a global normalization where the pixel intensities are scaled by maximum and minimum across the entire rotor blade as used by Jaroslawski et al. (Ref. 16). This allows for comparison across different runs, compensating for variations in heating. The normalization for each pixel with radial a chordwise location (r,x) is shown in equation 3.

$$I_N^{r,x} = \frac{I^{r,x} - min(I)}{max(I) - min(I)} \quad (3)$$

The second normalization (equation 4) scales the pixel intensities by the local maximum and minimum at each radial station, similar to the processing described by Thiessen (Ref. 15). This helps reveal the boundary layer structure but obscures the radial intensity differences between the root and tip of the blade. Equation 2 shows the normalization where each radial station is considered independently.

$$I_N^{r,x} = \frac{I^{r,x} - min(I^r)}{max(I^r) - min(I^r)} \quad (4)$$

5.2.1. Smooth configurations

Figure 10 shows the global normalized intensity across all three rotors at all three rotational velocities. All three rotors exhibit radial variation of intensity, with increased cooling toward the blade tips. additionally, all three rotors exhibit decreasing intensity along the leading edge as RPM increases due to the thinning of the attached laminar boundary layer.

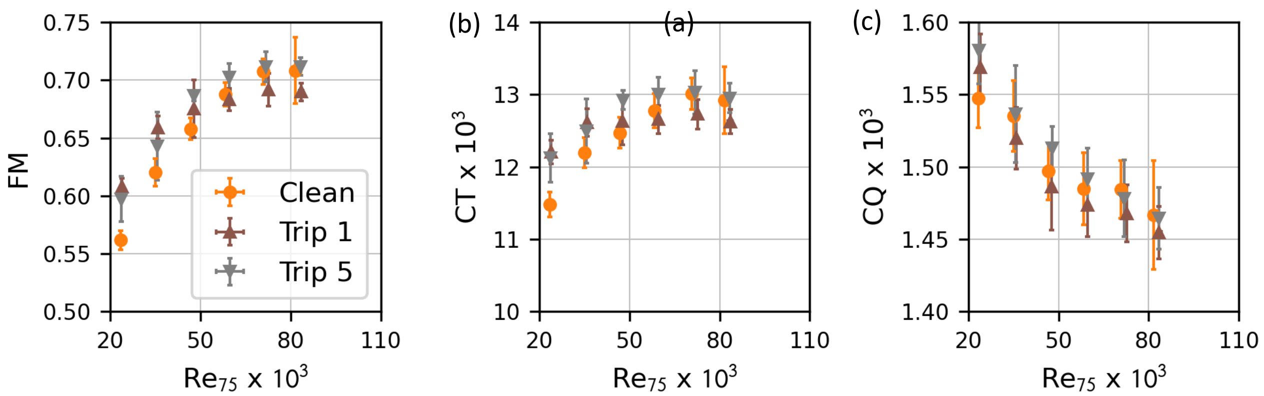

Figure 9. Comparison of clean IAI rotor with two trip configurations (a) Figure of merit vs. Reynolds Number (b) Thrust coefficient vs Reynolds number (c) Torque coefficient vs. Reynolds number

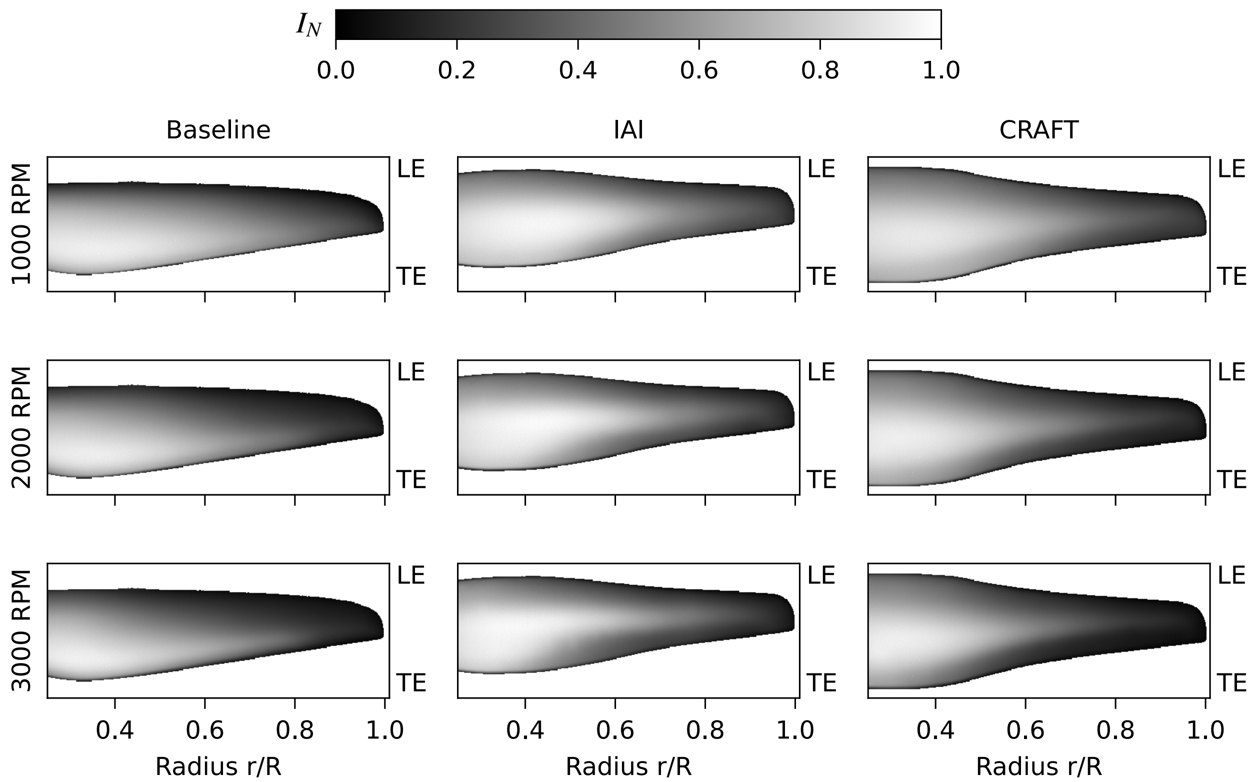

Figure 10. Global normalized IR intensity for baseline and clean optimized rotors at three rotational speeds, dark to light indicates low to high temperature

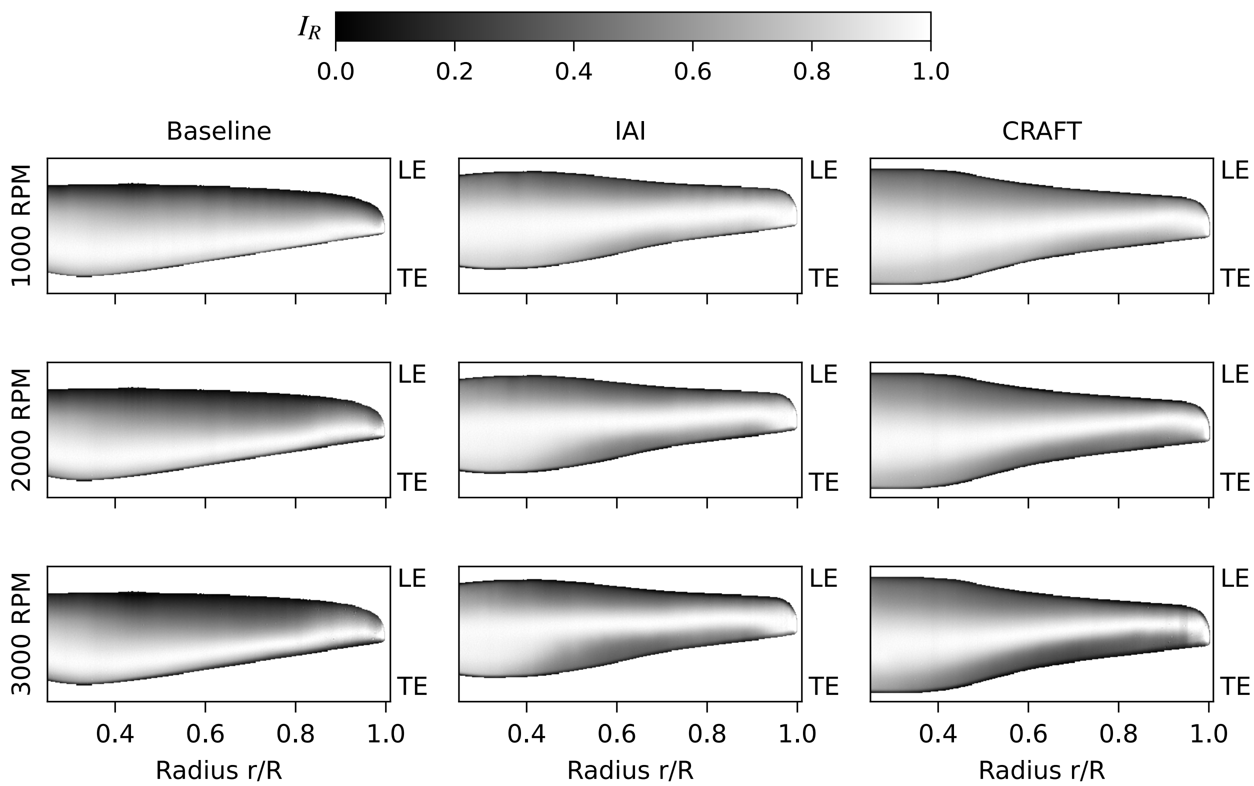

Figure 11. Radially normalized IR intensity for baseline and clean optimized rotors at three rotational speeds, dark to light indicates low to high temperature at each radial station

Beyond these similarities several differences appear between the baseline and optimized rotors. The baseline rotor inboard sections appear to show steadily increasing intensity from leading to trailing edge. In contrast both the IAI and CRAFT Tech rotor exhibit a temperature maximum near 50% chord and subsequent decrease toward the trailing edge, indicative of a separation bubble with subsequent transition.

The radially normalized data in Figure 11 helps to highlight these structural differences. Here we clearly see the mid-chord peak in the IAI and CRAFT Tech intensities extending from approximately 40% to 90% radius. As RPM increases the peak narrows indicating the shortening of the laminar separation bubble at higher Reynolds numbers. The baseline rotor peak intensity also narrows in the chordwise direction with increasing RPM but remains close to the rotor trailing edge.

Figure 12 presents radial slices of intensity extracted at 50%, 75% and 95% span. Each curve is averaged in the radial direction +-0.5% from the nominal station to smooth the trends. Following the analysis from Wynnychuck (Ref. 18) the shape of these intensity profiles can be related to boundary layer features for a laminar separation bubble with transition turbulent reattachment to within about 5% chord agreement with PIV as follows: From leading edge to trailing edge intensity increases as the laminar boundary layer grows. Separation is indicated by an inflection point and subsequent maximum slope dI_N/dx before the intensity maximum. Transition occurs downstream of the temperature maximum in the separated boundary layer near where the intensity slope dI_N/dx is minimum as the temperature decreases. Finally full turbulent reattachment occurs near where the intensity profile levels out with dI_N/dx approximately equal to zero.

At 1000 RPM only the CRAFT Tech rotor shows signs of transition and reattachment near 50% and 75% radius. The IAI rotor has a broad temperature peak near mid-chord with a gentle decreasing slope afterwards indicating transition but little substantial reattachment. The baseline rotor temperature peaks occur between 75% and 100% of the blade chord near

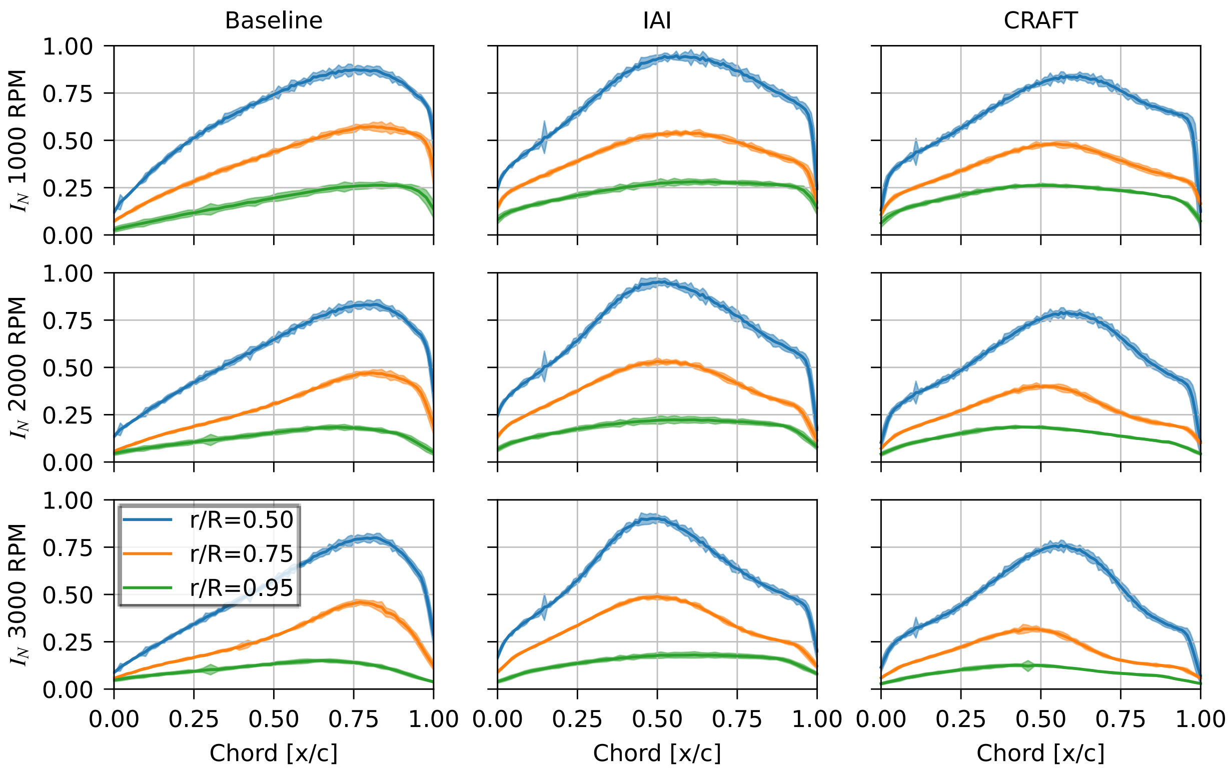

Figure 12. Chordwise profiles of global normalized intensity at three radial stations, data averaged over +-0.5% radius with shaded uncertainty bands representing +- 2 standard deviations

the trailing edge. There is a very small negative slope region at 50% span and nearly no negative slope at 75% span. The 95% span station for all three rotors show similar intensity profiles with a steady increase to a plateau that holds until very near the trailing edge. There is no indication of a separation bubble near the blade tips.

At 2000 and 3000 RPM the IAI and CRAFT Tech rotors show the first three of these features at 50% and 75% radius. There is an inflection point and maximum intensity slope, followed by the temperature peak, decrease, and a second inflection point. However, neither rotor exhibits the zero-slope intensity profile near the trailing edge indicative of fully reattached turbulent flow. In contrast the baseline rotor exhibits separation much further downstream near the trailing edge. At higher speeds the baseline rotor exhibits indications of transition, but there is no reattachment before the trailing edge. The 95% stations of all three rotor don't exhibit the temperature peaks associated with separation bubbles, likely due to interference form the tip vortex.

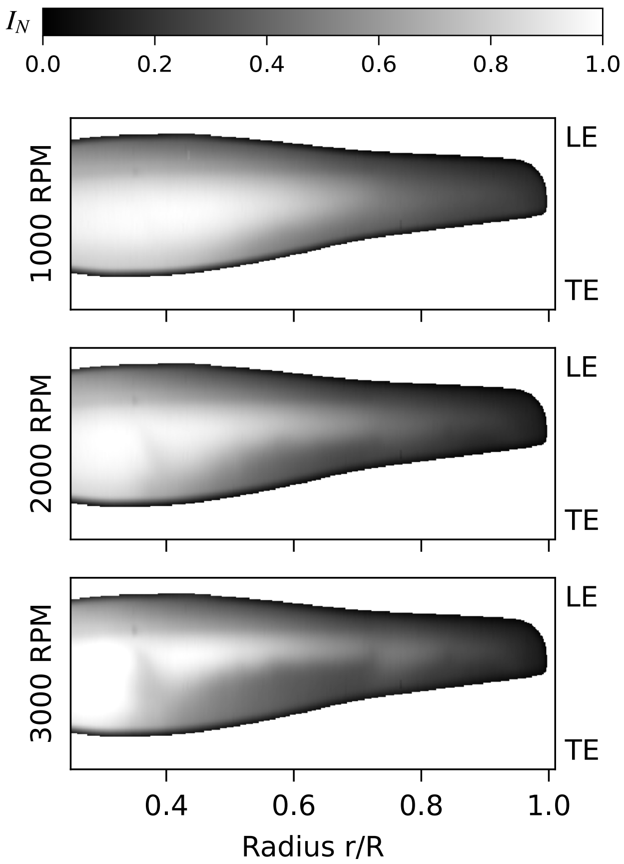

Figure 13. Global normalized IR intensity of the IAI rotor with trip #5 at three RPMs

5.2.2. IAI Tripped Configuration

IR measurements were taken of the IAI with the trip #5 configuration, shown to provide the best balance of performance across Reynolds numbers.

Figure 13 shows the global normalized temperature at all three rotor speeds. Turbulent wedges are seen originating from trip transitions at 40% and 75% radius, likely due to imperfections in the trip application. The low intensity region behind the separation bubble appears larger and darker than for the un-tripped rotor.

The difference between tripped and un-tripped intensity maps is presented in Figure 14 with red indicating regions of higher intensity and blue regions of lower intensity. This borrows from the differential in time (DIT) methodology which has been used to compare variations in time, azimuth angle, and blade pitch, highlighting otherwise small differences in absolute intensity (Ref. 15). Here the turbulent wedge at 40% radius and significantly stronger reattachment out to 75% radius are readily apparent as dark blue regions.

The chordwise profiles plotted in Figure 15 show much stronger transition and reattachment for the tripped rotor. The effect of the trip at 20% chord is readily apparent in the r/R = 0.5 curve exhibiting an inflection point near 25% chord. The effect of the trip is also seen downstream of the separation bubble where a stronger turbulent reattachment is indicated by the extended zero-slope region downstream of the intensity maximum. Meanwhile, the separation bubble at the 75% span location appears to be somewhat suppressed, with a smaller peak intensity compared to the un-tripped case shown in Figure 12.

5.3. Comparison with computational models

Both the IAI mid-fidelity and Helios CFD models were run for the baseline and IAI rotors in the clean, un-tripped configurations. Figure 16 shows the baseline rotor Figure of Merit, thrust coefficient and torque coefficient of the models compared to the experimental data. The MSES-VPM code significantly underpredicts FM, and misses the inflection point near 50,000 Re where the FM curve begins to level out. The Helios simulation does a better job, staying within experimental uncertainty up to 75,000 Reynolds number before slightly underpredicting the highest speed points. Looking at thrust and torque coefficient we see underprediction by both codes, although the shape of the curves is well captured by the Helios simulation.

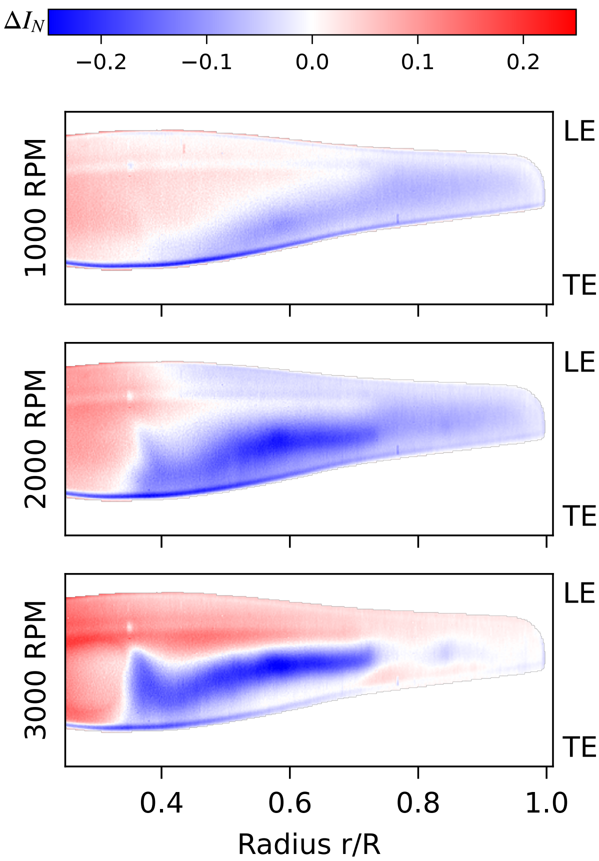

Figure 14. Differential thermography between IAI Trip #5 with clean, un-tripped IAI rotor. Blue represents cooler regions, white unchanged, and red hotter

The model results for the optimized IAI rotor are shown in Figure 17. Here the MSES-VPM code does a better job capturing both the value and shape of the figure of merit curve as well as the thrust coefficient when compared to predictions for the baseline rotor. The Helios prediction remains more accurate than the MSES-VPM code but is not as accurate with respect to the measured data as it is for the baseline rotor. This is likely because the Helios run parameters were based on a previous study of the impact of transition model on performance of the baseline T-Motor rotor (Ref. 22).

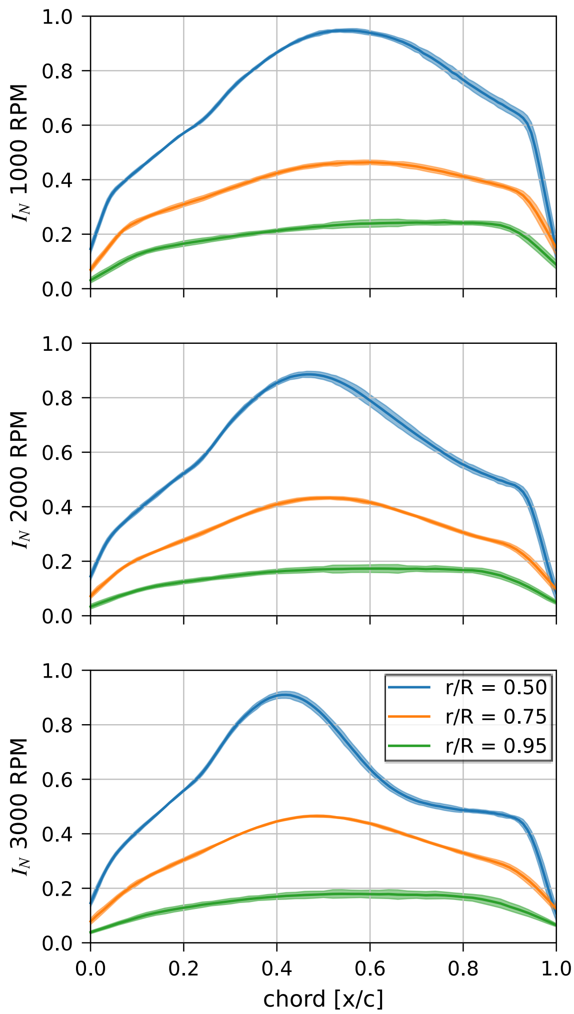

Figure 15. Chordwise profiles of global normalized intensity at three radial stations for the IAI rotor with trip #5 located at x/c = 0.2

The Helios and MSES-VPM codes predict nearly identical thrust coefficients for the IAI rotor, approximately 10-20% below the measured values. Both codes fail to predict the torque coefficient in both magnitude and trend. The measured data shows a near monotonic decreasing trend with Reynolds number, while both the Helios and MSES-VPM results predict that C_Q increases with Reynolds number. This indicates that there is a fundamental difference in the evolution of sectional drag with Re for the IAI rotor that is not captured by the models.

6. CONCLUSIONS

Two rotors were optimized for hover and forward flight performance with constraints based on the SUI endurance UAS as part of the U.S. Israel Rotorcraft Project Agreement. The final optimized designs were fabricated and tested in hover with measurements including thrust, torque and speed for performance calculations. IR thermography measurements were captured to analyze the structure of the rotor boundary layers. The effect of boundary layer tripping on the IAI optimized rotor performance and boundary layer was also explored.

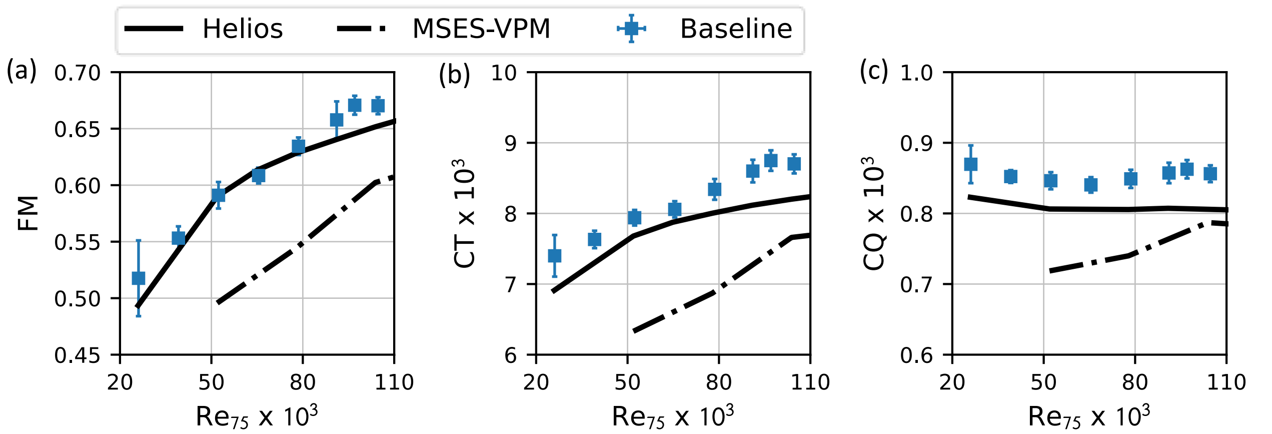

Figure 16. Comparison of baseline rotor experimental results to Helios and MSES-VPM computational models (a) Figure of merit vs. Reynolds Number (b) Thrust coefficient vs Reynolds number (c) Torque coefficient vs. Reynolds number

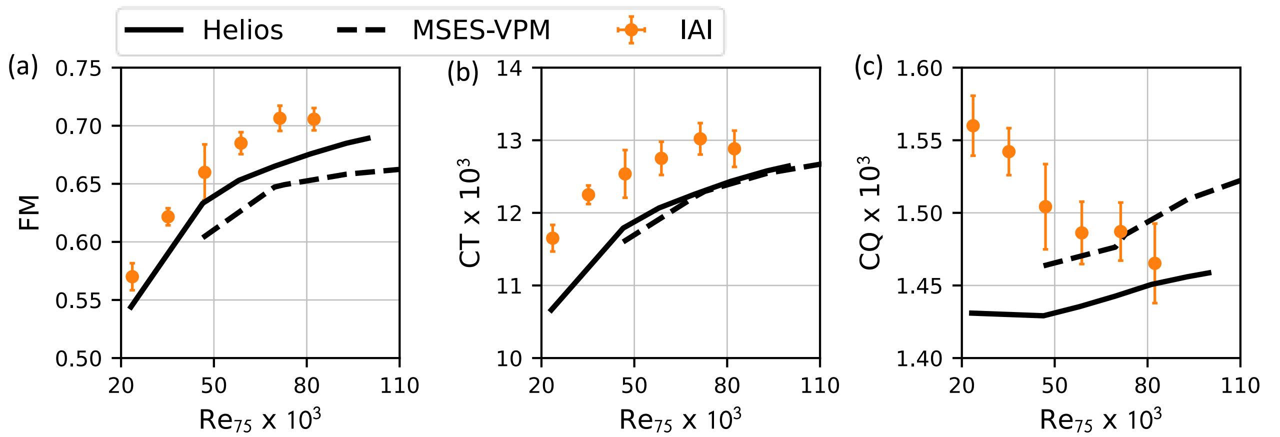

Figure 17. Comparison of IAI rotor experimental results to Helios and MSES-VPM computational models (a) Figure of merit vs. Reynolds Number (b) Thrust coefficient vs Reynolds number (c) Torque coefficient vs. Reynolds number

1. The two optimized rotors improved hover figure of merit by 3-6% over the baseline SUI endurance rotor
2. Both rotor optimization techniques converged to higher blade-loading designs with increased solidity, operating at 25-33% lower Reynolds number than the baseline rotor
3. Boundary layer trips applied to the IAI rotor improved performance at Reynolds numbers below 60,000, with some trip configurations exhibiting no performance penalty at higher Reynolds numbers
4. IR temperature measurements revealed transition/separation occurring near the trailing edge of the baseline rotor
5. Both optimized rotor IR measurements exhibited a separation bubble induced further upstream with a peak in intensity near mid-chord and subsequent transition and partial reattachment
6. IR measurements of the tripped rotor show evidence of stronger turbulent reattachment and a suppressed separation bubble compared to the un-tripped rotor
7. The mid-fidelity MSES-VPM model significantly underpredicts performance of the baseline rotor, while doing a better job capturing the trends of FM and thrust for the IAI rotor
8. The Helios CFD model captures the baseline rotor performance to within experimental uncertainty at lower Re, but has slightly larger performance discrepancy with the IAI rotor measurements
9. Both models fail to capture the measurement trend of falling torque coefficient with Reynolds number observed for the IAI rotor

Future work will include quantitative analysis of the measured IR intensity profiles to extract the separation and transition and reattachment locations. The inclusion of different transition models will be investigated to improve the CFD simulations to capture the physics associated with the laminar separation bubble. Additionally contours of skin friction coefficient can be extracted from the CFD results to compare with the IR measurements.

7. ACKNOWLEDGMENTS

The authors would like to acknowledge the U.S. Army 7- by 10-foot wind tunnel branch for assistance in experiment setup and execution. Thanks to James T. Heineck and the NASA Ames Fluid Mechanics Laboratory for lending the IR camera and acquisition computer, and for their help during initial setup. Also, thanks to Drs. David Schatzman and Manikandan Ramasamy for insightful discussions during data processing and analysis. The CRAFT Tech rotor optimization study was funded by a Phase II SBIR, "Design of Low Reynolds Number Rotors for UAS Applications," Contract No. W911W6-20-C-0039.

8. REFERENCES

1. Army UAS CoE Staff, “U.S. Army Unmanned Aircraft Systems Roadmap 2010-2035,” U.S. Army UAS Center of Excellence, Fort Rucker, Alabama, Apr. 2010.
2. J. H. McMasters and L. Henderson, “LOW-SPEED SINGLE-ELEMENT AIRFOIL SYNTHESIS,” *Science and Technology of Low Speed and Motorless Flight, Part 1*.
3. T. J. Mueller and J. D. DeLaurier, “AERODYNAMICS OF SMALL VEHICLES,” *Annual Review of Fluid Mechanics*, vol. 35, no. Volume 35, 2003. Annual Reviews, pp. 89–111, 2003. doi: https://doi.org/10.1146/annurev.fluid.35.101101.161102.
4. B. R. Hein and I. Chopra, “Hover Performance of a Micro Air Vehicle: Rotors at Low Reynolds Number,” *Journal of the American Helicopter Society*, vol. 52, no. 3, pp. 254–262, Jul. 2007, doi: 10.4050/JAHS.52.254.
5. M. Benedict, J. Winslow, Z. Hasnain, and I. Chopra, “Experimental Investigation of Micro Air Vehicle Scale Helicopter Rotor in Hover,” *International Journal of Micro Air Vehicles*, vol. 7, no. 3, pp. 231–255, Sep. 2015, doi: 10.1260/1756-8293.7.3.231.
6. W. J. Koning, E. A. Romander, and W. Johnson, “Optimization of Low Reynolds Number Airfoils for Martian Rotor Applications Using an Evolutionary Algorithm,” in *AIAA Scitech 2020 Forum*, Orlando, FL: American Institute of Aeronautics and Astronautics, Jan. 2020. doi: 10.2514/6.2020-0084.

7. M. S. Selig, “Low Reynolds Number Airfoil Design Lecture Notes”.
8. M. Drela, “Low-Reynolds-number airfoil design for the M.I.T. Daedalus prototype- A case study,” *Journal of Aircraft*, vol. 25, no. 8, pp. 724–732, Aug. 1988, doi: 10.2514/3.45650.
9. M. M. O’Meara and T. J. Mueller, “Laminar separation bubble characteristics on an airfoil at low Reynolds numbers,” *AIAA Journal*, vol. 25, no. 8, pp. 1033–1041, Aug. 1987, doi: 10.2514/3.9739.
10. J. Winslow, H. Otsuka, B. Govindarajan, and I. Chopra, “Basic Understanding of Airfoil Characteristics at Low Reynolds Numbers (104–105),” *Journal of Aircraft*, vol. 55, no. 3, pp. 1050–1061, May 2018, doi: 10.2514/1.C034415.
11. C. Christian Wolf, A. D. Gardner, and M. Raffel, “Infrared thermography for boundary layer transition measurements,” *Measurement Science and Technology*, vol. 31, no. 11, p. 112002, Nov. 2020, doi: 10.1088/1361-6501/aba070.
12. A. D. Overmeyer and P. B. Martin, “Measured Boundary Layer Transition and Rotor Hover Performance at Model Scale,” in *55th AIAA Aerospace Sciences Meeting*, Grapevine, Texas: American Institute of Aeronautics and Astronautics, Jan. 2017. doi: 10.2514/6.2017-1872.
13. J. Heineck, E. Schülein, and M. Raffel, “Boundary layer transition detection on a rotor blade using rotating mirror thermography”.
14. T. Norman *et al.*, “Fundamental Test of a Hovering Rotor: Comprehensive Measurements for CFD Validation,” in *Proceedings of the Vertical Flight Society 79th Annual Forum*, West Palm Beach, Florida USA: The Vertical Flight Society, May 2023, pp. 1–27. doi: 10.4050/F-0079-2023-17983.
15. R. Thiessen and E. Schülein, “Infrared Thermography and DIT of Quadcopter Rotor Blades Using Laser Heating,” in *The 15th International Workshop on Advanced Infrared Technology and Applications*, MDPI, Sep. 2019, p. 31. doi: 10.3390/proceedings2019027031.
16. T. Jaroslawski, M. Forte, J.-M. Moschetta, G. Delattre, and E. R. Gowree, “Characterisation of boundary layer transition over a low Reynolds number rotor,” *Experimental Thermal and Fluid Science*, vol. 130, p. 110485, Jan. 2022, doi: 10.1016/j.expthermflusci.2021.110485.
17. K. Richter, C. C. Wolf, A. Gardner, and C. B. Merz, “Detection of Unsteady Boundary Layer Transition Using Three Experimental Methods,” in *54th AIAA Aerospace Sciences Meeting*, San Diego, California, USA: American Institute of Aeronautics and Astronautics, Jan. 2016. doi: 10.2514/6.2016-1072.
18. D. W. Wynnychuk and S. V. Yarusevych, “Characterization of Laminar Separation Bubbles Using Infrared Thermography,” in *AIAA Aviation 2019 Forum*, Dallas, Texas: American Institute of Aeronautics and Astronautics, Jun. 2019. doi: 10.2514/6.2019-2808.
19. C. Russell, G. Willink, C. Theodore, J. Jung, and B. Glasner, “Wind Tunnel and Hover Performance Test Results for Multicopter UAS Vehicles,” National Aeronautics and Space Administration, Ames Research Center, NASA/TM 2018–219758, Feb. 2018.
20. N. S. Zawodny and N. A. Pettingill, “Acoustic Wind Tunnel Measurements of a Quadcopter in Hover and Forward Flight Conditions”.
21. C. R. Russell and M. K. Sekula, “Comprehensive Analysis Modeling of Small-Scale UAS Rotors”.
22. A. D. Thai, S. M. Grace, and R. Jain, “Effect of Turbulence Modeling Selection Within Helios for Small Quadrotor Aerodynamics,” *Journal of Aircraft*, vol. 59, no. 4, pp. 927–945, 2022, doi: 10.2514/1.C036410.
23. Y. Patel *et al.*, “Airfoils Design for the Low Reynolds Number Applications in Rotors,” in *AIAA AVIATION 2023 Forum*, San Diego, CA and Online: American Institute of Aeronautics and Astronautics, Jun. 2023. doi: 10.2514/6.2023-3244.
24. B. M. Adams *et al.*, “Dakota, A Multilevel Parallel Object-Oriented Framework for Design Optimization, Parameter Estimation, Uncertainty Quantification, and Sensitivity Analysis: Version 6.15 User’s Manual,” Nov. 2021, doi: 10.2172/1829573.
25. J. G. Coder, “Overview of the AFT Model for Transition Prediction in Complex Aerodynamic Flows,” in *IUTAM Laminar-Turbulent Transition*, S. Sherwin, P. Schmid, and X. Wu, Eds., Cham: Springer International Publishing, 2022, pp. 337–346.
26. A. Paszke *et al.*, “PyTorch: an imperative style, high-performance deep learning library,” in *Proceedings of the 33rd International Conference on Neural Information Processing Systems*, Red Hook, NY, USA: Curran Associates Inc., 2019.

27. G. S. Bir, “Structural Dynamics Verification of Rotorcraft Comprehensive Analysis System (RCAS),” Feb. 2005, doi: 10.2172/15011442.
28. A. Clarich, P. Geremia, S. Parashar, and R. Russo, “Use of Multivariate-Data-Analysis Techniques in modeFRONTIER for Efficient Optimization and Decision Making,” in *13th AIAA/ISSMO Multidisciplinary Analysis Optimization Conference*. doi: 10.2514/6.2010-9032.
29. M. Tugnoli, D. Montagnani, M. Syal, G. Droandi, and A. Zanotti, “Mid-fidelity approach to aerodynamic simulations of unconventional VTOL aircraft configurations,” *Aerospace Science and Technology*, vol. 115, p. 106804, Aug. 2021, doi: 10.1016/j.ast.2021.106804.
30. M. Drela, “A User’s Guide to MSES 3.05,” Massachusetts Institute of Technology, Dec. 2015.
31. A. Wissink *et al.*, “Recent Advancements in the Helios Rotorcraft Simulation Code,” Jan. 2016. doi: 10.2514/6.2016-0563.
32. V. Lakshminarayan, A. Wissink, R. Jain, and J. Sitaraman, “Improvements to Automated Strand Meshing Capabilities for Rotary Wing Applications,” in *Proceedings of the VFS International Transformative Vertical Flight 2020 Meeting*, San Jose, CA, Jan. 2020.